



## NUMERICAL ANALYSIS OF THE ACOUSTIC FIELD OF AN AXIAL FAN AT VARYING INFLOW CONDITIONS

Seyed Mohsen ALAVI MOGHADAM, Alexej POGORELOV,  
Benedikt ROIDL, Matthias MEINKE, Wolfgang SCHRÖDER

*Institute of Aerodynamics, RWTH Aachen University, Willnerstraße 5a,  
52062 Aachen, Germany*

### SUMMARY

The flow and the acoustic field of an axial fan is analyzed by a hybrid CFD/CAA method. In a first step, the tip clearance flow in a ducted axial fan is predicted by a large-eddy simulation (LES). The simulations are based on a multi-block structured finite volume method for a single blade using periodic boundary conditions in the circumferential direction. Computations are performed with undisturbed inflow as well as disturbed inflow conditions using a synthetic turbulence generation method. The turbulent interaction at the inlet dissipates the tip leakage vortex and triggers transition on a larger surface area of the blade. The acoustic field on the near field and the far-field is determined by solving the acoustic perturbation equations (APE) on a mesh for a single blade grid. The acoustic source terms are determined from the flow field results. The results from the CAA for the acoustic pressure field and noise spectra are in a good agreement with experimental data.

### INTRODUCTION

For axial fans the aerodynamically generated noise is typically dominant over mechanically generated noise from e.g. vibration or the noise caused by the motor. There are various aerodynamic sound sources generated by individual physical mechanisms [1]. For large tip clearances the flow from the pressure to the suction side of the blade creates a three-dimensional and possibly unstable tip vortex, which increases the boundary layer thickness on the suction side and the turbulence level on the blade and thus the emitted noise. The contribution of the flow field near the tip gap to the emission of the broadband noise has been shown by Jacob et al. [2] and Camussi et al. [3]. In addition, it was found that a quasi periodic interaction of the tip vortex with the downstream blade can generate broadened tonal noise components [4, 5]. Such noise can be reduced by minimizing the tip clearance [6]. Another important noise source is a non-uniform incoming flow to the fan. If the flow disturbance is steady, it will generate a purely periodic fluctuating blade loading and thus

generate narrow band tones at the blade passing and higher harmonic frequencies. A careful design of the inlet avoiding a non-axisymmetric flow field is necessary to reduce such noise, in real technical fan installation such sources usually cannot completely be avoided. The sound amplitude from such sources are, however, typically easier to predict than the broadband noise generated by non-uniform unsteady inflow such as a turbulent flow generated by some upstream obstacles. In this case, the emitted broadband sound pressure spectrum will depend on the details of the turbulence state of the incoming flow such as turbulent length and time scales. For small tip clearances, such noise is often dominating the sound spectrum for low speed axial fans. Although various models exist for the prediction of such broadband noise from unsteady fluctuations [7, 8, 9], the assumptions such as isotropy of the turbulence scales may not fulfilled, especially when the turbulence generating obstacles are mounted close to the fan blades. Another assumption often made is that the length scale of the turbulence is much larger than that of the blade chord, which is also not valid in many practical applications. Therefore, an attempt is made in this paper, to predict such sound from axial fans by resolving the major turbulence scales in the incoming flow by large eddy simulation and to predict the resulting sound field by a CAA method which uses sound sources from the flow field solution. This prediction method allows to predict the sound field by a minimum set of models for the turbulent flow and noise generation and as such should allow an accurate prediction of the noise level. The article possesses the following structure. First, the numerical methods are introduced. Second, the numerical setup and boundary conditions are presented. In the subsequent results section, a comparison of different flow field quantities of a 72° fan section with and without incoming turbulence are compared and the resulting acoustic fields are presented and compared to experimental data. Finally, the essential findings are summarized and some conclusions are drawn.

## NUMERICAL METHOD

### Hybrid LES/APE approach

An LES model based on a finite-volume method is used to simulate the compressible unsteady turbulent flow by solving the Navier-Stokes equations. The equations are spatially discretized by using the modified advection upstream splitting method (AUSM) [10]. A second-order 5-stage Runge-Kutta method is used for the temporal integration. A detailed description of the numerical methods, i.e., the discretization and computation of the viscous and inviscid fluxes is given by Meinke *et al.* [10]. For the LES the monotone integrated LES (MILES) approach [11] is adopted, i.e., the dissipative part of the truncation error of the numerical method is assumed to mimic the dissipation of the non-resolved subgrid-scale stresses. This solution method has been validated and successfully used, e.g., in [12, 13]. To deal with rotating components, the Navier-Stokes equations are formulated in a rotating frame of reference attached to the fan blade by using the relative time derivatives of the relative flow variables [14, 15]. The Coriolis acceleration and the centrifugal acceleration are considered as a source term in the momentum equations as well as the energy equation. To determine the sound propagation and to identify the dominant noise sources the acoustic perturbation equations (APE) are solved using a hybrid approach. A hybrid approach uses two steps to compute the acoustics. In the first step the flow field is computed within a small domain. This field is then used as the source to determine the acoustics within a larger domain. Since a compressible flow problem is considered, the APE-4 system, in which the perturbation density is eliminated by combining the energy and continuity equation, is used in a rotating frame of reference [16, 17]. To accurately resolve the acoustic wave propagation described by the APE-4 formulation, the acoustic perturbation equations are discretized in space using the 9-point 6th-order dispersion-relation preserving (DRP) scheme proposed by Tam & Webb [18] in the interior domain of integration and a special formulation of the DRP summation by parts scheme (SBP-DRP) [19] on the boundaries. A 4th-order alternating 5-6 stage low-dissipation and low-dispersion Runge-Kutta

method originally proposed by Hu *et al.* [20], and modified by Stanescu and Habashi [21] is applied for the temporal integration.

### Synthetic Turbulence Generation Method

To efficiently perform large-eddy simulations of a flow entering the CFD domain the concept of synthetic turbulence generation [22], which is an extension of the approach of [23], is used to prescribe the turbulent inflow field. To physically mimic the turbulence at the inlet plane a superposition of coherent structures is performed. These structures are generated over the LES inlet plane by superimposing virtual eddy cores, which are defined in a virtual volume downstream of the inlet plane which has the streamwise, the wall-normal, and the spanwise dimensions of the turbulent length scales. A detailed description of the reformulated synthetic turbulence generation formulation for flat plate simulations in zero, favorable, and adverse pressure gradients for Reynolds numbers based on the momentum thickness  $Re_\theta \leq 3500$  can be found in [22, 24].

## EFFECT OF THE INFLOW CONDITION ON THE FLOW AND THE ACOUSTIC FIELD

In this section, the flow through a rotating low Mach number axial fan is numerically investigated. The flow field is analyzed at a tip-gap width  $s/D_o = 0.001$  and a flow rate coefficient  $\Phi = \frac{4\dot{V}}{\pi^2 D_o^3 n} = 0.195$ . The diameter of the outer casing wall is  $D_o = 300$ mm and the inner diameter of the hub is  $D_i = 135$ mm. The rotational speed is  $n = 3000$  rpm. In the first part, the effect of a disturbed inflow condition using a synthetic turbulence generation method on the flow field is discussed and the findings are compared to the results imposing an undisturbed inflow condition [17]. All computations are performed at a fixed Reynolds number based on the rotational velocity and the diameter of the outer casing wall

$Re = \frac{\rho \pi D_o^2 n}{\eta} = 9.36 \times 10^5$  and a fixed Mach number  $M = \frac{\pi D_o n}{a_o} = 0.136$ . Here, the speed of sound is  $a_o = 346$  m/s. Subsequently, the acoustic field is discussed.

### Effect of the inflow condition on the flow field

A schematic view of the axial fan with and without a turbulence grid is shown in Fig. 1. The axial fan properties for the configuration with the turbulence grid, i.e., LES TG, match the axial fan properties for the configuration without the turbulence grid, i.e., LES. The fan has five twisted blades out of which only one has been resolved in the LES and CAA computations to reduce the computational costs.

(a)

(b)

Figure 1: Schematic view of the LES domain; (a) the ducted axial fan configuration; (b) the ducted axial fan configuration with a turbulence grid denoted by TG.

To provide the inflow data for the LES of the configurations, an additional LES to predict the flow downstream of the turbulence grid is performed using a flow solver, based on unstructured Cartesian meshes. The pattern width of the turbulence grid is defined by  $a \times a = 15 \times 15$  mm, and  $b \times b = 60 \times 60$  mm [25]. The computations were performed in the absolute frame of reference at a fixed volume flow rate  $V' = 0.650$  m<sup>3</sup>/s and a fixed Reynolds number  $Re = u_{ax} a / \nu = 9134.72$ , which is based on the mean axial velocity  $u_{ax}$  and the beam width of the grid, i.e.,  $a = 15$  mm. At the inflow, a fixed mass flow rate and a zero pressure gradient, whereas at the outflow a fixed static pressure and zero gradients for all other primitive variables are imposed. Three grids with approx.  $6.3 \times 10^6$ ,  $38 \times 10^6$ , and  $300 \times 10^6$  grid points were used to analyze the sensitivity of the numerical results with respect to the grid resolution. The mesh resolution on the beams for the finest grid is

approximately  $\Delta x_i/D_o \approx 9.9 \times 10^{-4}$ . For the simulations of the turbulence generating grid, the fan blades were neglected. Fig. 2(a) shows a computational mesh resolving the turbulence grid with approx. 300 million cells and Fig. 2(b) illustrates the instantaneous Q-criterion showing the vortical flow structures generated by the turbulence grid which are convected downstream.

(a) (b)

Figure 2: (a) Computational mesh of the LES domain; (b) Instantaneous vortical structures around the turbulence grid visualized by the Q-criterion and colored by magnitude of the relative velocity.

To focus more on the turbulent structures, the flow velocities in the x-, y-, and z-direction are shown in Fig. 3. They show large variations especially for the axial velocity component. To quantify the target inflow data to be used for the subsequent LES with the upstream turbulence grid, the time averaged radial distribution of the axial velocity and the axial velocity fluctuations from the LES are computed and compared with experimental data [26] in Fig. 4. An acceptable agreement between the numerical and experimental results for the grid generated turbulence is obtained. In the following, the flow field and turbulent statistics data are extracted to provide input for the synthetic turbulence generation.

The LES computation is performed using a synthetic turbulence generation method [22]. First, the mean velocity profile at the inflow obtained from the LES computation with the grid is averaged in time in the azimuthal direction, which enforces azimuthal periodicity. The target data contain the primitive variables, the radial velocity, the tangential velocity, and all components of the Reynolds stress tensor. Second, velocity fluctuations at the inflow are generated by a modified method proposed in [27]. A total number of 200 virtual eddies are seeded in a virtual box upstream of the fan at the inlet region. The virtual box comprises a  $72^\circ$  segment, starting at the inlet and extends to  $x/D_o=0.1333$ . Sponge layers are applied to reduce spurious hydrodynamic pressure fluctuations generated by the method.

Fig. 5 shows the multi-block structured LES mesh. The mesh size is approximately  $829 \times 521 \times 321$  in the streamwise, radial, and azimuthal direction. The tip-gap region for the configuration is resolved by allocating 21 grid points for the tip-gap sizes  $s/D_o = 0.001$ . The spatial steps based on the diameter of the outer casing wall in the streamwise, radial, and azimuthal direction are  $1.67 \times 10^{-4} \leq \Delta x/D_o \leq 1.67 \times 10^{-2}$ ,  $5.0 \times 10^{-5} \leq \Delta y/D_o \leq 1.67 \times 10^{-3}$ , and  $5.0 \times 10^{-5} \leq \Delta z/D_o \leq 7.67 \times 10^{-3}$ . On the blade surface and hub surface, a no-slip boundary condition is applied complemented by a zero normal pressure and density gradient and an adiabatic wall assumption. On the casing wall, a rotating

Figure 3: Instantaneous contours of absolute velocities in the x-, y-, and z-direction for the LES with grid generated turbulence.

(a) (b)

Figure 4: Time averaged radial distributions at the inlet of LES domain for the turbulent inflow configuration computed from the turbulence grid simulation; (a) axial velocity profile; (b) turbulence intensity of the axial velocity component.

boundary condition about the x-axis is imposed with maximum circumferential velocity  $U_\infty = \pi D_o n$ . At the inlet, an axial velocity profile corresponding to the experimental data [25] which satisfies a fixed volume flow rate and a zero-pressure gradient is imposed. Note that due to the measurements, the applied inlet velocity profile serves as a disturbance-free inflow through the axisymmetric AMCA nozzle located upstream of the fan test rig. At the outlet, a subsonic outflow boundary condition is applied with *a priori* known static pressure rise based on the performance curve of the

axial fan. A fully rotationally periodic boundary conditions including the symmetry line treatment is developed and imposed in the azimuthal direction. Moreover, a buffer zone is used far downstream of the blade for the outflow boundary to drive the instantaneous density and energy to the time averaged solution. A time step of  $\Delta t = 7.225 \times 10^{-4} D_o / U_\infty$  is chosen for the time integration, which is close to the stability limit of the explicit scheme. The fully developed flow field obtained after two full rotations of the rotor and data of another two full rotations were used for time averaging and the statistical analysis of the flow field. To be more precise, 10 snapshots per blade passing period during 2 fan rotations were recorded. In total, 1440 samples were used which required 8.6 TB of disc space. The simulation time was approx. 200 hours using 6000 cores for the LES computations.

(a) (b)

Figure 5: The multi-block structured mesh;  
(a) topology of the mesh; (b) mesh resolution on the hub and blade surface.

An overall view of the impact of inflow disturbances on the turbulent structures is shown in Fig. 6 which illustrates instantaneous contours of the  $\lambda_2$ -criterion [28] colored by the relative Mach number. The turbulent interaction at the inlet dissipates the tip leakage vortex and triggers transition on a larger surface area of the blade. This mechanism is observed in Fig. 7 which shows the development of the turbulence intensity along the blade chord denoted by  $x/c$ . Note that the turbulence intensity  $Tu$  is calculated inside the boundary layer thickness  $\delta$  and then integrated along the blade wall normal direction, i.e.,  $Tu = 100 * \frac{1}{\pi D_o n \delta} \int_0^\delta (\sqrt{\overline{u_x'^2} + \overline{u_r'^2} + \overline{u_\theta'^2}}) / 3 dn$ .

Figure 6: Instantaneous contours of the  $\lambda_2$ -criterion inside the ducted axial fan configuration color coded by the relative Mach number showing the vortical structures generated by the tip leakage flow for  $s/D_o=0.001$  at  $\Phi=0.195$ ; (top) undisturbed inflow; (bottom) turbulent inflow.

### Effect of inflow condition on the acoustic field

In the following, the acoustic field is numerically analyzed by the aforementioned hybrid CFD-CAA method. The source terms of the CAA computations are based on LES computations. The

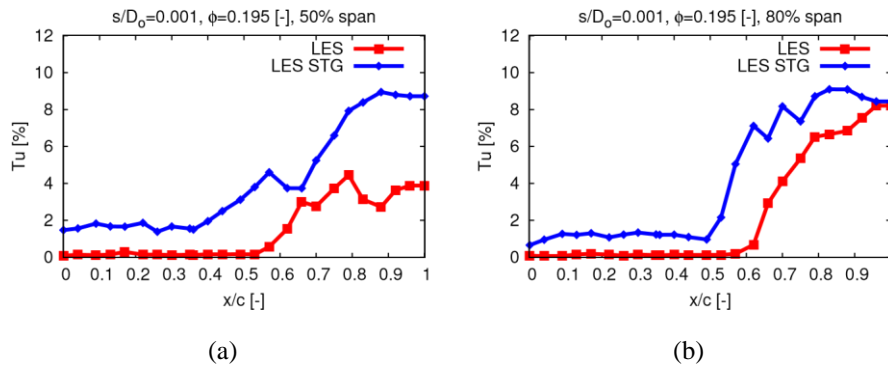


Figure 7: The time-averaged turbulent intensity distribution in several spanwise locations;  
(a) 50 % of span; (b) 80 % of span.

acoustic field is analyzed for the configurations with undisturbed and disturbed inflow. First, the effect of the undisturbed inflow condition on the acoustic field is discussed. Then, the effect of disturbed inflow condition on the acoustic field is analyzed.

### Analysis of the acoustic field at undisturbed inflow condition

In a second step, the acoustic field is predicted based on the corresponding LES results. A mesh approx.  $1060 \times 10^6$  grid points, which comprises a  $72^\circ$  segment of a rotating axial fan with periodic boundary conditions in the azimuthal direction is used. The computational mesh used for the LES is extended in the axial and radial direction up to  $20D_o$ . The grid spacing around the microphones positions is  $\Delta x_{mic}/D_o \approx 5 \times 10^{-3}$ , such that for 10 points per wavelength the maximum resolvable frequency is about 10 kHz. The time step of the acoustic analysis is  $\Delta t = 4.613 \times 10^{-3} D_o/a_o$  to ensure a fully stable numerical solution. The multi-block structured mesh for the acoustic domain resolving one out of five blades of the axial fan and a schematic view of the CAA computational setup are shown in Fig. 8(a) and Fig. 8(c).

The turbulent flow fields are determined for 24 full rotations, i.e., another 20 rotations are computed after the first 4 rotations that had been run for the flow field. The additional 20 rotations are based on a larger time step. Subsequently, the source terms are computed in the source region which contains approximately 122 million grid points with the same mesh resolution as the corresponding LES mesh. The source terms are computed based on 1500 LES snapshots at a time interval of  $\Delta t_{src} = 0.0224 D_o/a_o$ . The instantaneous distribution of the dominant fan noise source, which is the fluctuating Lamb vector  $\mathbf{L}' = (\boldsymbol{\Omega} \times \mathbf{u})'$ , for the two configurations is shown in Fig. 9(a). It is clearly visible that the strongest sources occur in regions with the highest turbulent kinetic energy, i.e., in the tip vortex, blade wake, and hub region. Moreover, the noise sources generated by the prescribed turbulent inflow exhibits higher amplitudes compared to the prescribed undisturbed inflow condition.

Based on the LES solution of the turbulent flow field, from which the acoustic sources are determined, the near far-field acoustics is computed by solving the APE-4 system. Since the contribution of entropy and non-linear terms can be neglected in this study, only the vortex sound sources, i.e., the fluctuating Lamb vector are taken into account. A least square optimized interpolation filter [29] using  $N = 10$  source samples is used for the source fields at every Runge-Kutta time-integration step. The acoustic computations are run for a non-dimensional time period of  $39 D_o/a_o$ . Explicit low-pass filtering at every 5th Runge-Kutta time-integration step is used to avoid numerical oscillations. Additionally, a sponge layer is used to damp acoustic wave reflections at the far-field and downstream of the fan.

(b) (c)

Figure 8: (a) Overall CAA mesh for the undisturbed inflow condition; (b) CAA mesh for the undisturbed inflow condition; (c) schematic view of the acoustic configuration of an axial fan showing the far-field microphone positions.

(a) (b)

Figure 9: Instantaneous contours of the Iso-surface of axial component of the fluctuating Lamb vector showing the major sound sources around the blade for the configuration with; (a) undisturbed inflow; (b) disturbed inflow.

In Fig. 10 the acoustic fields generated by the turbulent structures of the rotating axial fan for the two configurations are illustrated. The acoustic pressure field shows noise generation at a much higher frequency for the configuration LES TG and a noise generation at lower frequency for the configuration LES.

In the following acoustic analysis, the computed sound pressure spectra at the „circle C1“ which is defined in Fig. 11, are compared with the experimental data [26].

For the comparison of the numerical results with the experimental data, the acoustic signals are analyzed on circle C1, which are located 1.30m upstream of the inlet of the fan. The acoustic measurements were carried out in the fixed frame of reference. To compare the computed sound spectra in the rotating frame of reference with the experimental findings, 1001 probes are equally distributed on each circle. First, the position of the microphones are calculated in the fixed frame of reference and then sound pressure spectrum for all processed microphones are computed. Finally,

(a) (b)  
*Figure 10: Instantaneous contours of the fully developed acoustic field for the configurations;*  
*(a) undisturbed inflow; (b) turbulent inflow.*

(a) (b)  
*Figure 11: Evaluation method for microphone data; (a) fixed frame; (b) rotating frame,*  
*and schematic of the virtual microphone positions for the two acoustic configurations.*

the sound pressure spectrum of all microphones are averaged. The sound pressure spectra on the circle C1 is shown in Fig. 12. The evaluation of the sound pressure level on the circle C1 shows a convincing agreement especially at the broadband noise level. However, the computed sound pressure level in the lower frequencies deviate from the experimental measurements. This is probably due to the fact that a one-blade acoustic simulation using periodic boundary conditions lack certain low wave number mode which is clearly observable in the corresponding spectral analysis.

### Analysis of the acoustic field at disturbed inflow condition

The influence of disturbed inflow condition on the acoustic field for the configuration with the turbulent inflow is investigated. The multi-block structured mesh for the acoustic domain resolving one out of five blades of the axial fan is illustrated in Fig. 8(b). A mesh with approx.  $1082 \times 10^6$  grid points, which comprises a  $72^\circ$  segment of a rotating axial fan, with periodic boundary conditions in the azimuthal direction is used. Note that the turbulence grid is not resolved in the computational mesh. Based on the LES solution of the turbulent flow field for the configuration LES TG, from which the acoustic sources are determined, the near far-field acoustics is computed by solving the APE-4 system. Fig. 9(b) illustrates the instantaneous distribution of the dominant fan noise source, which is the fluctuating Lamb vector  $\mathbf{L}' = (\boldsymbol{\Omega} \times \mathbf{u})'$ , for the configurations with turbulent inflow. The incoming turbulent field triggers transition on almost the whole surface of the blade and produces pronounced sound sources near the fan blade. Instantaneous contours of the fully developed acoustic field is depicted in Fig. 12(b). The acoustic pressure field for the configuration with the turbulent inflow shows the noise generation at a much higher frequency in comparison with the acoustic pressure field for the configuration undisturbed inflow due to a much higher level of turbulent activities generated in the flow field. To quantify the computed sound spectra, the sound pressure spectra on the circle C1 for the both aforementioned configurations are shown in Fig. 12.

(a) (b)  
*Figure 12: Sound spectra on the circle C1;*  
*(a) configuration with undisturbed inflow; (b) configuration with turbulent inflow.*

The sound pressure spectra for the configuration turbulent inflow underpredicts the sound pressure level especially in low frequency range (below 1 kHz). This is probably caused by assuming

isotropic turbulence in the synthetic turbulence generation method. Additionally, the assumption of periodic conditions in the azimuthal direction can not capture low wave number components close to the symmetry axis of the fan and influences the low frequency acoustic part. Therefore, it gives motivation to investigate the influence of periodic boundary conditions on the turbulent scales in the disturbed inflow conditions.

## CONCLUSION

The flow and the acoustic field of a ducted axial fan were simulated by a hybrid CFD/CAA method. First, the flow field was computed by an LES and subsequently, the acoustic field was determined by solving the APE. For the axial fan, two configurations with a tip gap  $s/D_o = 0.001$  at the flow rate coefficient  $\Phi = 0.195$  were performed and the results were compared to experiment [26]. The configuration with the turbulence inflow was simulated by separately computing the turbulence generating grid and the rotating blades. The time and azimuthal average of the velocity profile from the computation of the turbulence generating grid superposed with synthetic turbulence were then used as inflow condition for the computation of the fan blade. The findings showed that the turbulent interaction at the inlet dissipates the tip leakage vortex and triggers transition on a larger surface area of the blade. The most intense noise sources occur in regions with the highest turbulent kinetic energy, i.e. in the tip vortex, blade wake and near the hub region. In the second step, the acoustic field was determined in rotating frame of reference. The overall agreement of the pressure spectrum and its directivity with measurements confirms the correct identification of the sound sources and accurate prediction of the acoustic duct propagation. Using a periodic condition could not resolve low wave number contributions in the spectral analysis. However, in agreement with experimental data, the results show that the prescribed turbulent inflow increases the broadband noise level.

## ACKNOWLEDGMENT

The research has received funding by the German Federal Ministry of Economics and Technology via the “*Arbeitsgemeinschaft industrieller Forschungsvereinigungen Otto von Guericke e.V.*” (AiF) and the “*Forschungsvereinigung Luft- und Trocknungstechnik e.V.*” (FLT) under the grant no. 17747N (L238). Computing resources were provided by the High Performance Computing Center Stuttgart (HLRS) and by the Jülich Supercomputing Center (JSC).

## REFERENCES

- [1] I.Jr. Sharland. *Sources of noise in axial flow fans*. Journal of Sound and Vibration, 1(3):302–322, **1964**.
- [2] M.C. Jacob, J. Grilliat, R. Camussi, and G. Caputi Gennaro. *Aeroacoustic investigation of a single airfoil tip leakage flow*. International Journal of Aeroacoustics, 9(3):253–272, Feb **2010**.
- [3] R. Camussi, J. Grilliat, G. Caputi-Gennaro, and M. C. Jacob. *Experimental Study of a Tip Leakage Flow: Wavelet Analysis of Pressure Fluctuations*. Journal of Fluid Mechanics, 660:87–113, **2010**.
- [4] A. Pogorelov, M. Meinke, and W. Schröder. *Cut-Cell Method Based Large-Eddy Simulation of Tip-Leakage Flow*. Physics of Fluids, 27(7):075106, **2015**.

- [5] T. Zhu, D. Lallier-Daniels, M. Sanjosé, S. Moreau, and T. H. Carolus. *Rotating coherent flow structures as a source for narrowband tip clearance noise from axial fan*. AIAA Paper 2016, 2822, **2016**.
- [6] T. Zhu. *On the Flow Induced Tip Clearance Noise in Axial Fans*. Dr.-Ing. Diss. Univ. Siegen, Shaker Verlag, ISBN 978-3-8440-4802-5, **2016**.
- [7] M. Schneider and T. Carolus. *Turbulent Ingestion Noise form Axial Fans - Statistic Parameters of the Inflow and Noise Prediction*. Proc. of the 12th Int. Congress on Sound and Vibration, Lisbon, **2005**.
- [8] T. Carolus, M. Schneider, and H. Reese. *Axial flow fan broad-band noise and prediction*. Journal of Sound and Vibration, 300(1-2):50–70, **2007**.
- [9] H. Reese, C. Kato, and T.H. Carolus. *Berechnung von akustischen Quellen eines NiederdruckAxialventilators bei hochturbulenter Zustromung*. VDI BERICHTE, 1922:29, **2005**.
- [10] M. Meinke, W. Schröder, E. Krause, and T. Rister. *A comparison of second-and sixth-order methods for large-eddy simulations*. Computers & Fluids, 31(4):695–718, **2002**.
- [11] J. P. Boris, F. F. Grinstein, E. S. Oran, and R. L. Kolbe. *New insights into large eddy simulation*. Fluid Dynamics Research, 10(4-6):199–228, **1992**.
- [12] N. Alkishriwi, M. Meinke, and W. Schröder. *A large-eddy simulation method for low Mach number flows using preconditioning and multigrid*. Computers and Fluids, 35(10):1126–1136, **2006**.
- [13] M. Konopka, M. Meinke, and W. Schröder. *Large-Eddy Simulation of Shock-Cooling-Film Interaction*. AIAA Journal, 50:2102–2114, **2012**.
- [14] J. P. Veuillot and L. Cambier. *Computation techniques for the simulation of turbomachinery compressible flows*. Twelfth International Conference on Numerical Methods in Fluid Dynamics, January **1990**.
- [15] *CFD Validation for Propulsion System Components*. ISBN 92-836-1075-X/NASA19980203585, **1998**. RTO/STO Technical Report AGARD-AR-355.
- [16] R. Ewert and W. Schröder. *Acoustic perturbation equations based on flow decomposition via source filtering*. Journal of Computational Physics, 188(2):365–398, **2003**.
- [17] S. M. Alavi Moghadam, M. H. Meinke, and W. Schroeder. *Analysis of the Acoustic Field of a Ducted Axial Fan*. In *23rd AIAA/CEAS Aeroacoustics Conference*, page 3873, **2017**.
- [18] C.K.W. Tam and J.C. Webb. *Dispersion-relation-preserving finite difference schemes for computational acoustics*. Journal of Computational Physics, 107(2):262–281, **1993**.
- [19] S. Johansson. *High order finite difference operators with the summation by parts property based on DRP schemes*. Division of Scientific Computing, Department Information Technology, Uppsala University, Sweden, **2004**. Technical Report 2004-036.
- [20] F.Q. Hu, M.Y. Hussaini, and J.L. Manthey. *Low-dissipation and low-dispersion Runge–Kutta schemes for computational acoustics*. Journal of Computational Physics, 124(1):177–191, **1996**.
- [21] D. Stanescu and W.G. Habashi. *2N-storage low dissipation and dispersion Runge-Kutta schemes for computational acoustics*. Journal of Computational Physics, 143(2):674–681, **1998**.

- [22] B. Roidl, M. Meinke, and W. Schröder. *A reformulated synthetic turbulence generation method for a zonal RANS-LES method and its application to zero-pressure gradient boundary layers*. International Journal of Heat and Fluid Flow, 44:28–40, **2013**.
- [23] M. Pamies, P. Weiss, E. Garnier, S. Deck, and P. Sagaut. *Generation of synthetic turbulent inflow data for large eddy simulation of spatially evolving wall-bounded flows*. Physics of Fluids (1994-present), 21(4):045103, **2009**.
- [24] B. Roidl, M. Meinke, and W. Schröder. *Boundary layers affected by different pressure gradients investigated computationally by a zonal RANS-LES method*. International Journal of Heat and Fluid Flow, 45:1–13, **2014**.
- [25] T. Zhu. *Akustische Nachrechnung von Ventilatoren Hauptarbeitspaket C, durchgeführt an der Universität Siegen: Aeroakustisches Validierungs experiment. Abschlussbericht, AiF16773N/2FLT L236, 2012*.
- [26] T. Zhu and T. H. Carolus. *Experimental and numerical investigation of the tip clearance noise of an axial fan*. Proceedings of ASME Turbo Expo 2013 (GT2013-94100), San Antonio, Texas, USA, **2013**.
- [27] P. Batten, U. Goldberg, and S. Chakravarthy. *Interfacing Statistical Turbulence Closures with Large-Eddy Simulation*. AIAA Journal, 42(3):485–492, **2004**.
- [28] J. Jeong and F. Hussain. *On the Identification of a Vortex*. Journal of Fluid Mechanics, 285:69– 94, **1995**.
- [29] G. Geiser, S. R. Koh, and W. Schröder. *Analysis of Acoustic Source Terms of a Coaxial Helium/Air Jet*. AIAA Paper 2011-2793, **2011**.